Photon scattering from ^{12}C and ^{4}He nuclei near the $\Delta(1232)$ resonance

R. Igarashi, J. C. Bergstrom, H. S. Caplan, K. G. E. Doss,* E. L. Hallin, and D. M. Skopik
Saskatchewan Accelerator Laboratory, University of Saskatchewan, 107 North Road, Saskatoon, Saskatchewan S7N 5C6, Canada

D. Delli Carpini, E. C. Booth, E. K. McIntyre, and J. P. Miller
Department of Physics, Boston University, 590 Commonwealth Avenue, Boston, Massachusetts 02215

M. A. Lucas, B. E. MacGibbon, A. M. Nathan, and D. Wells
Department of Physics, University of Illinois at Urbana-Champaign, Nuclear Physics Laboratory, Champaign, Illinois 61820

(Received 18 April 1995)

Angular distributions for photon scattering from ^{12}C and ^{4}He have been measured using continuous wave bremsstrahlung from the Saskatchewan Accelerator Laboratory pulse stretcher ring. Data for carbon were taken at 158.8, 195.2, 197.2, 247.2, and 290.2 MeV end-point energies, and for helium were taken at an end-point energy of 158.8 MeV. A large NaI(Tl) gamma ray spectrometer with 1.7% resolution was used to detect the scattered photons at laboratory scattering angles, ranging from 20° to 150°. The excellent energy resolution of the NaI detector allowed a separation of elastic from inelastic photon scattering for the first time at these energies. The angular distributions for elastic scattering are in only fair agreement with delta-hole theory and theory based on the optical theorem at forward angles, and completely disagree with theory at backward angles. Measured cross sections for inelastic scattering leading to the 4.43 MeV state in carbon are small compared to the elastic scattering at forward angles, but are dominant at backward angles. This experiment is the first to separate elastic from inelastic photon scattering at these energies.

PACS number(s): 25.20.Dc, 14.20.Gk

I. INTRODUCTION

The first excited nucleon resonance is the $\Delta(1232)$. It has been extensively studied by pion scattering and is a dominant feature in photon scattering. The $\Delta(1232)$ also manifests itself in complex nuclei, leading Koch *et al.* [1] to develop a delta-hole model to account for its excitation in photon scattering reactions. This model assumes that the incident photon primarily excites a delta-hole intermediate state which then propagates within the nucleus, finally decaying into a photon. The model takes into account nuclear medium effects such as the production, propagation and decay of the delta through Fermi motion, Pauli blocking, and intermediate coherent pion propagation.

The first test of the delta-hole model for elastic photon scattering was attempted by Hayward and Ziegler [2] who scattered 150–400 MeV photons from carbon at 115°. Their experiment, which did not have sufficient resolution to resolve elastic from inelastic scattering, disagreed in magnitude with the calculations of Koch *et al.* Subsequent calculations by Vesper *et al.* [3] and Arenhovel *et al.* [4] suggested that in the Hayward and Ziegler experiment, inelastic scattering should dominate over elastic scattering, thus perhaps explaining the discrepancy with the delta-hole model of [1].

In another test of the delta-hole model, Austin *et al.* [5] measured the angular distribution at 180 MeV for photon scattering from helium. Their measurement also disagreed with the Koch *et al.* delta-hole calculation: the forward angle data were slightly below the model prediction, and the backward angle point was much higher than the theory. Because of these unexpected results, a large NaI high resolution spectrometer was constructed [6] and a new measurement at the peak of the Δ resonance (320 MeV) was performed again on ^{4}He [7]. Only forward angle cross sections were obtained in this new experiment, which agreed with the delta-hole model predictions. The disagreement at the backward angles was still unresolved. More extensive photon scattering measurements on ^{4}He by Delli Carpini *et al.* [8] were subsequently performed, and these confirmed the earlier work of Austin *et al.*, namely that the backward angle cross sections are much higher than theory. It has been suggested that the enhancement in the cross section in ^{4}He at backward angles and at low energies is due to the effect of meson exchange currents (MEC) [9,10].

This paper reports new measurements of Compton scattering on carbon and helium. By using the high resolution NaI spectrometer of [6], the elastic and inelastic scattering channels in ^{12}C were resolved. This permits us, for the first time, to make a meaningful compari-

*Present address: Regina General Hospital, Nuclear Medicine Department, 1400 14th Avenue, Regina, Saskatchewan Canada, S4P 0W5.

son with modern calculations of Compton scattering from complex nuclei.

II. EXPERIMENTAL METHOD

Differential cross sections for photon scattering by ^{12}C and ^{4}He were measured at the Saskatchewan Accelerator Laboratory (SAL) at incident electron energies of 158.8, 195.2, 197.2, 247.2, and 290.2 MeV. The experimental setup in the area termed $EA2$ is shown in Fig. 1. The electron beam was produced by the 300 MeV linac and the duty factor was increased to over 50% by the pulse stretcher ring (EROS) and then used to generate bremsstrahlung in a 0.01 radiation length aluminum radiator. A dipole magnet swept the post-bremsstrahlung electrons into a beam dump. The photons were then collimated by a tapered lead collimator, and a downstream sweep magnet removed any charged particles that were produced in the collimator. The photon flux was measured by a Wilson type quantameter [11] situated at the end of the photon beam dump. The useful photon intensity produced in this way is far greater than that available using tagged photons, and this increased intensity was essential in measuring the small photon scattering cross sections with a relatively small solid angle detector.

Scattered photons were detected by the Boston University NaI gamma ray spectrometer [6]. This spectrometer is a 26.7 cm diameter cylindrical core of NaI surrounded by 10.8 cm thick quadrant crystals of NaI. Six 12.7 cm thick annular plastic scintillators around the circumference of the NaI, and three 2.54 cm thick flat plastic scintillators in front and back of the NaI, provided cosmic ray background rejection with 98% efficiency. Cosmic rays could also be identified by comparing relative energy deposition in the quadrants and the core of the NaI. Additional data cuts based on this comparison resulted in an overall cosmic ray rejection efficiency of 99.995%, with a loss of photon scattering events of less than 1%. The detector was shielded by a box with 18 cm thick walls made of lead and steel, surrounded by 36 cm of borated wax.

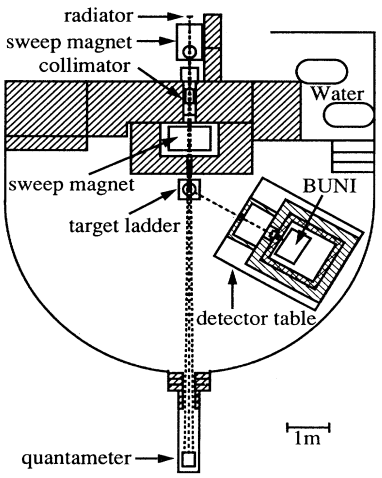

FIG. 1. A scale diagram of the photon-scattering experimental area at SAL, showing the Boston University NaI detector "BUNI" and its shielding consisting of 18 cm of lead and steel surrounded by 36 cm of borated wax.

A 12.7 cm diameter tungsten ring inserted into an aperture in the shielding box was used to define the angular acceptance of the detector. Pulse pileup was reduced by placing a 22.9 cm thick beryllium cylinder in the aperture defined by the tungsten ring to absorb low energy photons entering the spectrometer. Charged particles entering the aperture were vetoed by three thin plastic scintillators, two in front of the beryllium plug and one behind the plug. Shielding was installed around the thin scintillators in the aperture which served to precollimate the tungsten ring defining the detector solid angle.

For angle changes, the detector and shielding moved on airpads. Since $EA2$ was not large enough at this time to accommodate the full angular range around a fixed target, the target was also moved along the beam line.

Carbon measurements were alternated with helium measurements [8] since the helium spectra provided a secondary, unambiguous energy calibration. Two carbon targets were used, one 3.98 g/cm^2 thick, the other 1.60 g/cm^2. The choice of target thickness depended on photon-induced background rates which are highest at forward angles. Typically, for angles forward of 60°, the background rate was high enough to require low beam fluxes and the thinner target. Beyond 90°, there was usually little or no background, so the thick target was used. The target was turned so that its normal bisected the detector angle.

Typically, data were acquired over 4 to 8 h for each angle, with total incident photon fluxes of about 10^{11} photons/MeV in the particular region of interest. Beam flux was limited by the pulse pileup of the high energy photons by the more numerous low energy background photons. Background rates were inferred from low energy (0.5 MeV threshold) trigger rates, and pileup was monitored by observing distortions in the shape of pedestal spectra.

III. DATA ANALYSIS

A. Detector calibration

For each incident energy, the detector was placed directly in the beam line and an extremely low bremsstrahlung flux was measured. The absolute energy calibration of the core of the detector was then determined by fitting an EGS4 [12] simulated photon spectrum to the measured zero degree spectrum. The Matthews and Owens model [13] of bremsstrahlung spectra was used as input to the EGS simulation because of its accuracy in predicting the shape of the spectrum near the end point. The success of these fits, shown in Fig. 2, is further confirmation. The NaI quadrants were calibrated by measuring gamma ray spectra from a radioactive source whenever angles were changed. A xenon flasher gain-monitoring system was then used to compensate for run-

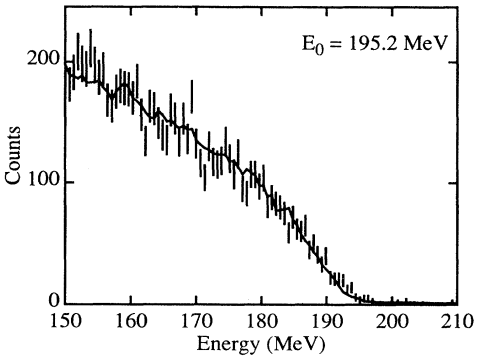

FIG. 2. A representative zero degree bremsstrahlung spectrum measured with BUNI for an end-point energy of 195.2 MeV. The solid line is an EGS4 simulation, normalized to the data, using the Matthews and Owens bremsstrahlung spectrum [13].

by-run gain variations. This system consisted of a xenon flasher delivering light flashes to the NaI segments via fiber optics, and also to a small reference NaI to which a radioactive source was attached. Before processing scattered photon data, ADC outputs for flasher events were extracted and gains were compensated, on a run-by-run basis. The uncertainty in the energy calibrations was estimated to be 0.5% with this technique.

B. Data reduction

Pulse height signals from each of the 19 photomultipliers on the NaI spectrometer were scaled by the respective energy calibration factors and then were combined to produce quadrant, core, and total energies.

No hardware vetoes were applied during data acquisition. Instead, veto counter signals were converted by ADCs and rejection decisions were made in offline software. Threshold cuts on the cosmic ray veto counters and a cut on the ratio of quadrant to total energy eliminated cosmic rays. The thresholds on the veto counters at the detector collimator eliminated charged particle events entering the spectrometer.

The data analysis system [14] was used to generate scattered-photon energy histograms which were written to files on a run-by-run basis. Histogram files were grouped and summed according to target, angle, and energy, and the cosmic ray background was subtracted. The summed "target out" histograms were then subtracted from the "target in" histograms to produce the final background subtracted histograms from which yields, and hence cross sections, could be extracted.

C. Elastic cross section extraction

Cross sections were extracted according to the formula

$$\left.\frac{d\sigma}{d\Omega}(\theta_{\mathrm{c.m.}},\bar{E})\right|_{\mathrm{c.m.}} = \frac{C(E_1,E_2)\tau(E_1,E_2)}{N_t\Omega N_\gamma(E_1,E_2)\varepsilon(E_1,E_2)} \times J(\theta,\bar{E}) \ , \quad (1)$$

where E_1 and E_2 define a "region of interest" (ROI) in the incident photon spectrum; C (the yield) is the number of detected photons in a range that corresponds to the incident ROI, kinematically corrected for target recoil using the Compton formula; τ is the fraction of photons in the ROI that are not absorbed en route to the quantameter; N_t is the number density of target nuclei; Ω is the spectrometer solid angle; N_γ is the number of incident photons in the ROI as measured by the quantameter; ε is the detector efficiency for the ROI; J is the Jacobian for transforming the differential cross section from the laboratory frame to the center-of-momentum frame, and $\bar{E}$ is the bremsstrahlung weighted mean energy of the ROI.

A simulation of a detected photon spectrum is shown in Fig. 3, illustrating a problem in extracting yields in bremsstrahlung experiments. The photon spectrum is a continuum which can make identification of specific scattering channels difficult. The extraction of elastic yields relied on resolving a ROI in scattered spectra that contained only elastically scattered photon events. The major competing reaction was neutral photopion production with the pion decaying to two photons, but the maximum energy for these photons is always 15–30 MeV lower than the maximum energy of elastically scattered photons. This leaves a 15–30 MeV region for inclusive photon scattering. An elastically scattered photon carries more energy than an inelastically scattered photon that leaves the target nucleus in an excited state. This defines a region of strictly elastically scattered photons at the end point, with a width corresponding to the excitation energy of the first excited state. For helium, this region is 20 MeV wide, making it possible to obtain high statistical accuracy. For carbon, this region is 4.43 MeV, due to the 4.43 MeV (2^+) excited state. The detector resolution at 250 MeV is 4 MeV, making the extraction of cross sections very sensitive to errors in energy calibration and also limiting the statistical accuracy. As a result, only upper limits could be set for those measurements with

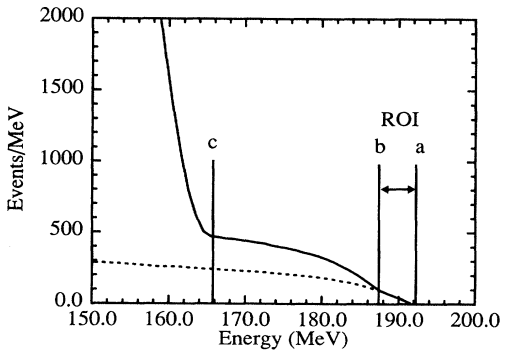

FIG. 3. A simulation of the detected photon spectrum for carbon at 90°, for E_0 = 195 MeV. The dashed line represents the elastic scattering while the solid line is the sum of all channels including π^0 decay. *a* is the elastic scattering end point, *b* is the inelastic scattering end point for the first excited state, *c* is the neutral pion decay photon end point. The region of interest (ROI) for elastic scattering is bounded by *a* and *b*.

very low elastic scattering cross sections. These restrictions naturally make the ^{12}C measurements much more difficult to analyze than the ^{4}He data. The ROI for ^{12}C was chosen to be 4.4 MeV wide, with the upper limit situated at the bremsstrahlung end point. The ^{4}He data at 155 MeV were analyzed with a ROI of 15 MeV width, with the upper limit 5 MeV below the bremsstrahlung end point.

An EGS4 simulation of the target and detector setup was used to estimate the absorption of photons by material within the solid angle of the NaI detector and to estimate the detector efficiency. These simulations indicated that the net fraction of scattered photons detected for the ^{12}C cross sections was only 30% to 40%, due to those two effects. The beryllium plug in the detector collimator absorbed 50% of the scattered photons in the ROI that would have entered the NaI. The detector efficiency was 60% to 80%, mainly due to the narrowness of the 4.4 MeV ROI relative to the detector energy resolution. Figure 4 is a simulation of a typical high energy NaI response function at 190 MeV and shows the large fraction of the photon yield that is lost with a 4.4 MeV ROI.

The acceptance solid angle was determined by a separate EGS4 Monte Carlo simulation of photon scattering from an extended target through the detector's collimator.

The quantameter measured the total energy of the incident photon beam, allowing the photon flux (N_γ) between photon energies E_1 and E_2 to be estimated using the model bremsstrahlung spectrum of Matthews and Owens [13] in the expression

$$N_\gamma(E_1, E_2) = U_q Q \frac{\int_{E_1}^{E_2} A(E) n(E) dE}{\int_0^{E_0} A(E) n(E) E \, dE} , \qquad (2)$$

where Q is the charge collected by the quantameter, U_q is the quantameter calibration constant, $n(E)$ is the photon spectral distribution, $A(E)$ is the photon absorption function, and E_0 is the end point energy of the bremsstrahlung.

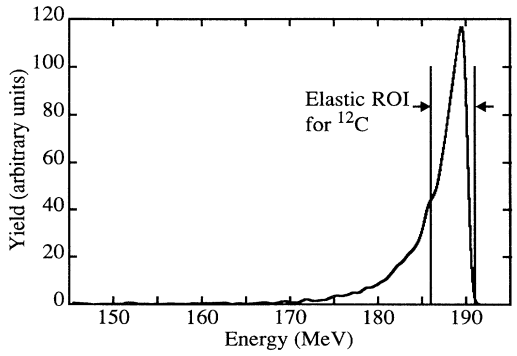

FIG. 4. EGS4 simulated detector response function for BUNI for 190 MeV photons. The region of interest (ROI) for elastic scattering is constrained by the first excited state, and reduces the detector efficiency to 60–80 %.

The number density of the carbon target varied because the target was rotated to a new angle for each NaI detector angle. The number density of the helium target did not vary with the detector angle since its orientation was fixed with respect to the photon beam line.

The reduction of photon flux to the quantameter [τ in Eq. (1)] and the reshaping of the spectrum of the primary beam [$A(E)$ in Eq. (2)] by the target and other material in the beam, was modeled by EGS4 simulations of the beam line.

When the large (20 MeV) ROI for helium was divided up into 5 MeV subregions, cross sections for the end point region were inconsistent with cross sections for low energy regions. Since these cross sections should be a continuous function of energy, they were extracted with 0.2% adjustments to the energy calibration until continuity in the helium cross sections was achieved. Since the carbon and helium measurements were alternated, the calibration adjustments from helium could also be applied to the carbon data. The final accuracy in the energy calibration is 0.3%.

D. Inelastic cross section extraction

Elastic and inelastic scattering spectra for carbon are shown in Fig. 5. For some spectra, especially at angles forward of 60°, the elastic channel was so large that reliable inelastic yields could not be extracted.

In the spectra where there was significant inelastic strength, modeled scattered spectra were used to fit the elastic and inelastic channels. The model consisted of a sum of simulated detected spectra, corresponding to elastic and inelastic kinematics for the scattered photons. The transitions to and from the intermediate states were assumed to be mainly dipole ($\Delta J = 1$). Therefore,

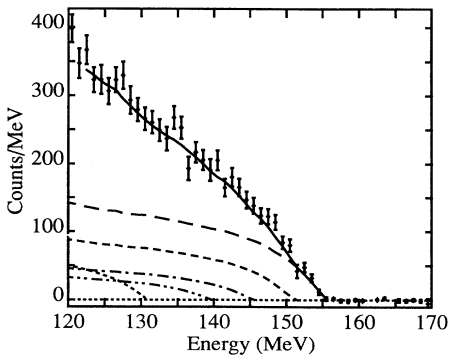

FIG. 5. A fit to the scattered photon spectrum from carbon at 120° and 158.8 MeV end-point energy, including inelastic scattering contributions. The solid curve is a sum of spectra from all scattering channels, while the long-dashed curve is the elastic scattering spectrum. The short-dashed curve describes inelastic scattering to the 4.43 MeV state. The dash-dotted curve represents inelastic scattering to the 10.3 MeV state; the dash-dot-dotted curve represents inelastic scattering to the 16.11 MeV state, and the dotted curve represents inelastic scattering to the 25.18 MeV state.

TABLE I. Differential cross sections for inelastic scattering from the 4.43 MeV state of carbon.

Bremsstrahlung weighted average lab energy (MeV)	c.m. angle	Differential cross section (μb/sr)	Statistical (μb/sr)	Systematic (μb/sr)
154.0	90.6	0.0378	0.0126	0.0088
	120.7	0.0645	0.0189	0.0151
	145.7	0.0510	0.0242	0.0119
189.4	60.8	0.181	0.053	0.042
	91.2	0.0576	0.0192	0.0135
	121.1	0.0869	0.0288	0.0203
	150.5	0.0375	0.0135	0.0088
191.4	91.0	0.0705	0.0278	0.0165
	105.6	0.149	0.048	0.035
	132.4	0.0498	0.019	0.0117
	144.4	0.0670	0.0248	0.0157
239.5	105.9	0.176	0.101	0.041
	120.7	0.0217	0.0155	0.0051
	130.3	0.0294	0.0215	0.0069
	147.2	0.0295	0.0187	0.0069
280.6	67.1	0.235	0.118	0.055
	91.1	0.115	0.0451	0.0269
	121.4	0.0399	0.0192	0.0093

TABLE II. Inclusive differential cross sections for scattering from carbon (10 MeV ROI). Asterisks indicate value is an upper limit.

Bremsstrahlung weighted average lab energy (MeV)	c.m. angle	Differential cross section (μb/sr)	Statistical error (μb/sr)	Systematic error (μb/sr)
137.1	20.2	0.345	0.049	0.019
	40.7	0.254	0.017	0.014
	60.3	0.162	0.006	0.009
150.9	20.3	0.418	0.091	0.035
	40.7	0.314	0.029	0.026
	60.4	0.226	0.011	0.019
172.5	19.0	1.14	0.11	0.06
	30.4	1.01	0.07	0.05
	45.6	0.630	0.031	0.034
	60.8	0.392	0.014	0.021
174.5	30.4	1.06	0.05	0.06
186.3	19.0	1.82	0.20	0.15
	30.5	1.42	0.11	0.12
	45.7	0.887	0.054	0.075
	60.8	0.423	0.022	0.036
188.3	30.5	1.70	0.09	0.14
225.6	20.4	7.95	0.43	0.043
	30.7	4.79	0.20	0.26
	45.9	2.30	0.12	0.12
	60.9	0.668	0.029	0.036
236.4	20.4	13.5	0.8	1.1
	30.7	6.21	0.36	0.52
	45.9	2.64	0.19	0.22
	61.0	0.687	0.046	0.058
271.1	20.5	14.1	1.3	0.8
	30.8	8.23	0.47	0.44
	46.0	2.46	0.15	0.13
	67.0	0.297	*	
277.5	20.5	17.7	1.5	1.5
	30.8	9.03	0.51	0.76
	46.0	2.98	0.17	0.25
	67.0	0.173	*	

0^+ and 2^+ excited states at 4.43, 7.65, 10.3, 16.11, and 25.18 MeV were used in these fits (see Fig. 5). These states were chosen because they have even spin and even parity, and photon scattering was assumed to proceed primarily via $E1$ or $M1$ intermediate transitions. The parameters from the elastic and inelastic fits were used to reconstruct spectra for each channel and yields were extracted from those reconstructions in a manner similar to the elastic yields. The main difference was in the computation of the kinematics, where the excitation energy was absorbed by the recoiling nucleus. However, only the yields for the first excited state were reliable. For the inelastic channels to higher excitations, the compounding systematic uncertainties gave too much freedom to individual channels in the fitting procedure. Nonetheless, inclusion of the additional states *in combination* was required to account for the overall shape of the scattered photon spectrum and the significant excess yield below the elastic region.

E. Pulse pileup analysis

While pileup was kept at acceptable levels for most of the experiment, some of the spectra were found, during off-line analysis, to be contaminated by pileup. Additional analysis was performed to determine how much and to what level these data were affected. During the experiment, a wave-form digitizer recorded the pulse shape from the NaI for each event. The spectra compiled from the digitizer gave a good indication of the presence of pileup; however, the resolution of the digitizer was insufficient for determining the shape of a pileup pulse smaller than 3 MeV, so the net pileup rate could not be determined.

Pileup data appear above the kinematic end point of the scattered bremsstrahlung spectra. The level of pileup was obtained from fits to these spectra. The fitting technique was similar to the inelastic cross section analysis, but included a simulated pileup spectrum. For some of

TABLE III. Angular distributions of differential cross sections for carbon. Asterisks indicate value is an upper limit.

Bremsstrahlung weighted average lab energy (MeV)	c.m. angle	Differential cross section (μb/sr)	Statistical error (μb/sr)	Systematic error (μb/sr)
154.0	20.3	0.454	0.236	0.061
	40.7	0.410	0.075	0.055
	60.4	0.272	0.085	0.036
	90.6	0.180	0.017	0.024
	120.7	0.120	0.012	0.016
	145.7	0.0976	0.0123	0.0131
189.4	19.0	2.26	0.39	0.30
	30.5	1.23	0.21	0.16
	45.7	0.841	0.120	0.113
	60.8	0.364	0.045	0.049
	91.2	0.0695	0.0054	0.0093
	121.1	0.0273	0.0075	0.0037
	150.5	0.00565	0.00296	0.00076
191.4	30.5	1.74	0.21	0.23
	91.0	0.115	0.013	0.015
	105.6	0.0337	0.0138	0.0045
	132.4	0.0274	0.0064	0.0037
	144.4	0.0146	0.0053	0.0020
239.5	20.4	14.3	1.8	1.9
	30.7	6.78	0.79	0.91
	46.0	2.96	0.46	0.40
	61.0	0.691	0.109	0.093
	92.2	0.327	0.100	0.077
	105.9	0.0952	*	
	120.7	0.0867	*	
	130.3	0.0479	*	
	130.3	0.0393	0.0150	0.0053
	147.2	0.0378	0.0146	0.0051
280.6	20.5	15.6	3.7	2.1
	30.9	7.89	1.18	1.06
	46.0	3.29	0.40	0.44
	67.1	0.123	*	
	91.1	0.0821	*	
	121.4	0.0431	*	
	145.4	0.0140	*	

the data the elastic events were completely overwhelmed by pileup, in which case only upper limits could be assigned for cross sections. For the remaining data, pileup levels could be calculated and the yields corrected.

F. Systematic errors

The major sources of systematic error in most cases where the quantameter calibration and the NaI energy calibration.

The energy calibration was known to 0.3%. This man-

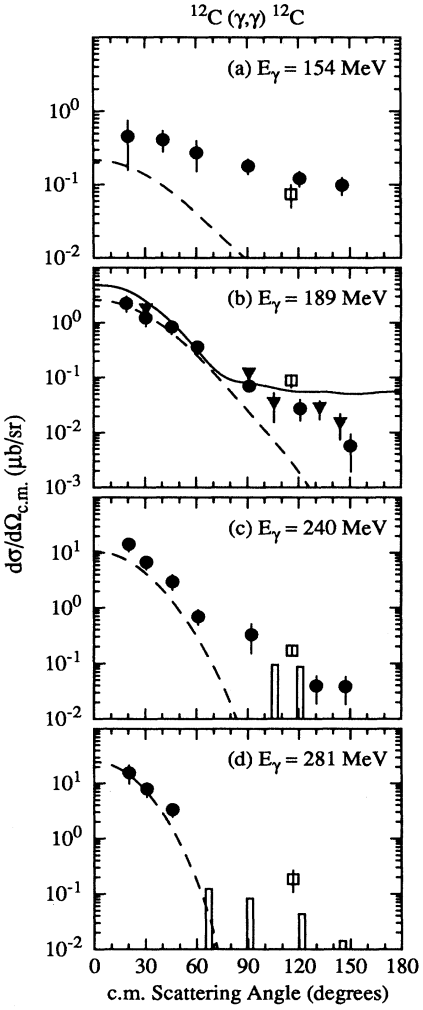

FIG. 6. Differential cross section for elastic photon scattering from carbon as a function of c.m. scattering angle. The circles and triangles are present data. [The circles and triangles in (b) describe data at 189.4 and 191.4 MeV, respectively.] Vertical bars where shown are upper limit estimates from the present measurements for data that were effected by pileup. The open squares are the Hayward and Ziegler results [2] at 150, 200, 250, and 300 MeV. The solid line is a delta-hole calculation by Koch *et al.* [1]. The dashed line is a schematic calculation as described in text.

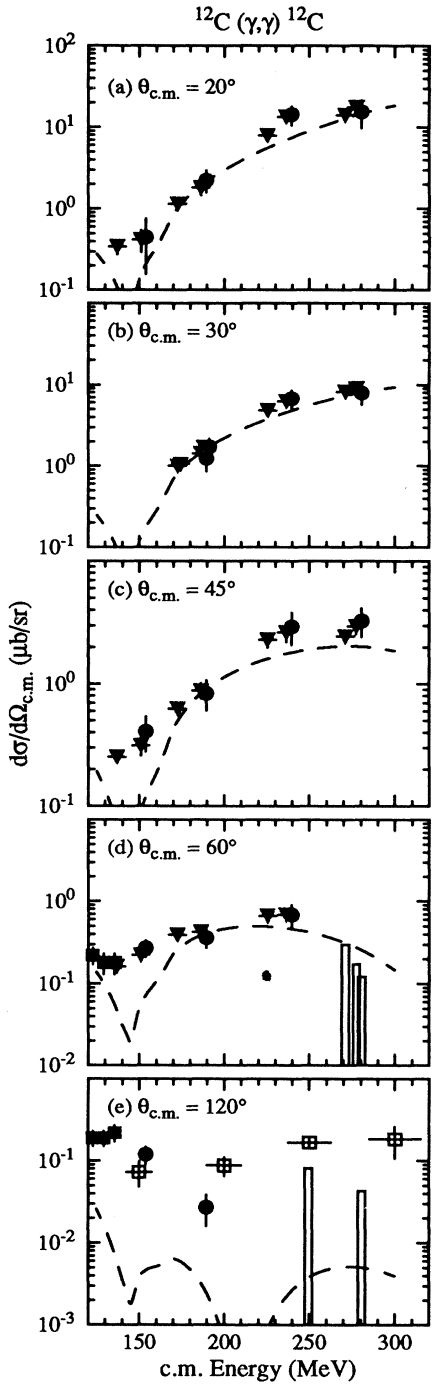

FIG. 7. Differential cross section for elastic photon scattering from carbon as a function of c.m. energy. The circles derive from a 4.4 MeV wide ROI (region of interest) at the end point, while the triangles are from a 10 MeV wide ROI assuming no inelastic contributions above pion threshold. Vertical bars are upper limit estimates for both domains. The solid squares represent the data of Schelhaas *et al.* [18], while the open squares are from Hayward and Ziegler [2]. The dashed line is a schematic calculation as described in the text.

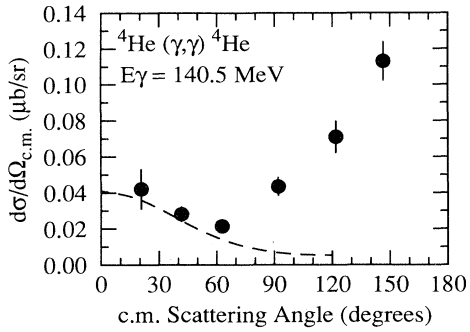

FIG. 8. Differential cross section for elastic photon scattering from helium at 140.5 MeV. Circles are the present data. The dashed line is a schematic calculation as described in the text.

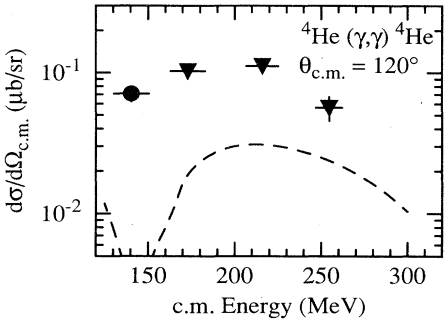

FIG. 9. Differential cross section for elastic photon scattering from helium at 120° (c.m.). The circle is the present result. Triangles are from Delli Carpini *et al.* [8]. The dashed line is a schematic calculation as described in the text.

ifests itself as a 10% uncertainty in cross sections for carbon, due to the largest gradient at the end point of the bremsstrahlung spectrum and the narrowness of the 4.4 MeV wide ROI (cf. Table I). For the cross sections at forward angles with a 10 MeV wide ROI (cf. Table II), the uncertainty due to calibration was 5% for the higher energy ROI, and 2% for the lower energy ROI. For the helium data, the combination of a wider ROI, with the upper limit well below the end point, translated to a 1% uncertainty in the cross section.

The quantameter was calibrated against a standard NBS P2 chamber at SAL. The uncertainty for the quantameter calibration was estimated to be 3%.

For those cross sections where pileup corrections were required, an additional 20% error was estimated from the range of the fits and the uncertainty in the simulated pileup spectra.

Inelastic scattering yields from the first excited state had an estimated 10% additional uncertainty, again due to the range of fits. The uncertainty for the second excited state was 50%, and 100% for subsequent individual levels. It should be noted that these uncertainties are for the individual excitations in the scattered spectra. The good fit to the data, however, confirms the abundance of inelastically scattered photons and the chosen strengths for inelastic scattering from higher levels.

IV. RESULTS AND DISCUSSION

A. Carbon

Figure 6 shows the measured c.m. angular distributions for elastic photon scattering by carbon at four photon energies; these data are also tabulated in Table III. The theoretical curves are the delta-hole calculation by Koch *et al.* [1], for $E_\gamma = 200$ MeV, and a "schematic" model calculation at all energies. The schematic model uses the optical theorem and dispersion relations to determine the scattering amplitudes at zero degrees, from which the cross section at other angles were obtained [15–19]. It is given by

$$\frac{d\sigma}{d\Omega}(E,\theta) = \frac{d\sigma}{d\Omega}(E,0)|F(q)|^2\frac{(1+\cos^2\theta)}{2} ,$$

where $F(q)$ is the form factor determined from electron scattering.

At forward angles, both models agree with the data. For the schematic predictions, this is expected since the optical theorem dictates the photon scattering amplitude at zero degrees.

At backward angles, both models disagree with the data. For a photon energy of $E_\gamma = 189$ MeV, the delta-hole model prediction overestimates the cross section, while the schematic model underestimates it. This is different from the situation in ^{4}He Compton scattering reported by Delli Carpini [8]. In that case the delta-hole model greatly underestimated the cross section in the back angle region. This discrepancy may be due to MECs which have not been taken into account in the delta-hole model [9].

The energy dependence of the cross sections is shown in Fig. 7. At the higher energies our data at 120° are lower than those of Hayward and Ziegler [2] which were taken at 115°. This strongly suggests that their results include excited-state contributions which were excluded by the better energy resolution of the NaI detector used in this experiment. The results of Schelhaas *et al.* [18] from 122–135 MeV agree with these new cross sections.

B. Helium

Figure 8 shows the measured angular distribution for helium at 140.5 MeV (see also Table IV). These data are an extension of the measurements reported by Delli Carpini *et al.* [8]. Note that the cross section at back angles exceeds the forward angle cross section. This is in complete disagreement with the trend of both the delta-hole and the schematic model predictions but is quite similar to the proton Compton scattering reported by Hallin *et al.* [20]. With the success of dispersion calculations in describing those data, similar calculations may also be able to describe the high backward angle cross sections for ^{4}He. The energy dependence of these ^{4}He

TABLE IV. Angular distributions of differential cross sections for helium.

Bremsstrahlung weighted average lab energy (MeV)	c.m. angle	Differential cross section (μb/sr)	Statistical error (μb/sr)	Systematic error (μb/sr)
140.5	20.8	0.0421	0.0090	0.0019
	41.6	0.0282	0.0027	0.0012
	62.8	0.0215	0.0020	0.0009
	92.0	0.0435	0.0031	0.0019
	121.8	0.071	0.006	0.003
	146.5	0.113	0.006	0.005

data at 120° in the region of the delta are shown in Fig. 9 along with the earlier low energy data from Delli Carpini.

V. CONCLUSIONS

Differential cross sections for photon scattering from ^{12}C and ^{4}He have been measured with a high resolution gamma ray spectrometer that ensured total rejection of neutral pion background and good separation of elastic from inelastic events.

The elastic angular distributions for carbon near 200 MeV agree with a delta-hole calculation at forward angles, but disagree at backward angles, thus demonstrating that the present delta-hole calculation is deficient for ^{12}C. At forward angles a schematic calculation, based upon the optical theorem, is in general agreement with the results for both ^{12}C and ^{4}He.

These new measurements provide an important test of models of the delta resonance. Future measurements on carbon at the delta resonance will be particularly interesting, since predictions for helium seem to be in fair agreement with the available data. It would also be interesting to see if the behavior in carbon and helium below the delta resonance, as reported here, is similarly reflected at energies above resonance.

ACKNOWLEDGMENTS

We gratefully acknowledge the efforts of the staff and students at the Saskatchewan Accelerator Laboratory. During the initial phase of this experiment Dr. P. C.-K Kuo and Dr. C. Rangacharyulu made important contributions that led to the success of these measurements. We would also like to thank Dr. Evans Hayward, Dr. E. L. Tomusiak, Dr. H. Arenhovel, Dr. J. Ahrens, and Dr. F. Wissman for very informative discussions. This work was supported by the Natural Sciences and Engineering Research Council of Canada (NSERC) and the United States National Science Foundation (NSF).

[1] J. H. Koch, E. J. Moniz, and N. Ohtsuka, Ann. Phys. (N.Y.) **154**, 99 (1984).
[2] E. Hayward and B. Ziegler, Nucl. Phys. **A414**, 333 (1984).
[3] J. Vesper, D. Drechsel, and N. Ohtsuka, Phys. Lett. **159B**, 233 (1985).
[4] H. Arenhovel, M. Weyrauch, and P. G. Reinhard, Phys. Lett. **155B**, 22 (1985).
[5] E. J. Austin, E. C. Booth, E. K. McIntyre, J. P. Miller, B. L. Roberts, D. A. Whitehouse, and G. Dodson, Phys. Rev. Lett. **57**, 972 (1986).
[6] J. P. Miller, E. J. Austin, E. C. Booth, K. P. Gall, E. K. McIntyre, and D. A. Whitehouse, Nucl. Instrum. Methods Phys. Res. **270**, 431 (1988).
[7] E. J. Austin, E. C. Booth, D. Delli Carpini, K. P. Gall, E. K. McIntyre, J. P. Miller, D. Warner, and G. Dodson, Phys. Rev. Lett. **61**, 1922 (1988).
[8] D. Delli Carpini *et al.*, Phys. Rev. C **43**, 1525 (1991).
[9] A. I. L'vov and V. A. Petrunkin, *Perspectives on Photon Interactions with Hadrons and Nuclei*, Proceedings of the Workshop, Göttingen, 1990, edited by M. Schumacher and G. Tamas (Springer-Verlag, Berlin, 1990), pp. 124–144.
[10] M. Weyrauch, Nucl. Phys. **A480**, 425 (1983).
[11] Robert R. Wilson, Nucl. Instrum. Methods **1**, 101 (1957).
[12] Walter Nelson, Hideo Hirayama, and David Rogers, *The EGS4 Code System*, SLAC Report 265 (1985).
[13] J. L. Matthews and R. O. Owens, Nucl. Instrum. Methods **111**, 157 (1973).
[14] *Lucid Data Acquisition and Analysis System User's Guide* (Saskatchewan Accelerator Laboratory, 1991).
[15] E. G. Fuller and E. Hayward, Phys. Rev. **101**, 692 (1956).
[16] E. Hayward, *Photonuclear Reactions*, N. B. S. Monograph 118 (1970).
[17] W. Pfeil, H. Rollnik, and S. Stankowski, Nucl. Phys. **B73**, 166 (1974).
[18] K. P. Schelhaas, Nucl. Phys. **A506**, 307 (1990).
[19] J. Ahrens, Nucl. Phys. **A446**, 229 (1985).
[20] E. L. Hallin *et al.*, Phys. Rev. C **48**, 1497 (1993).